Telescopes Alignment Using the Sharpness Function Method Based on Undersampled Images
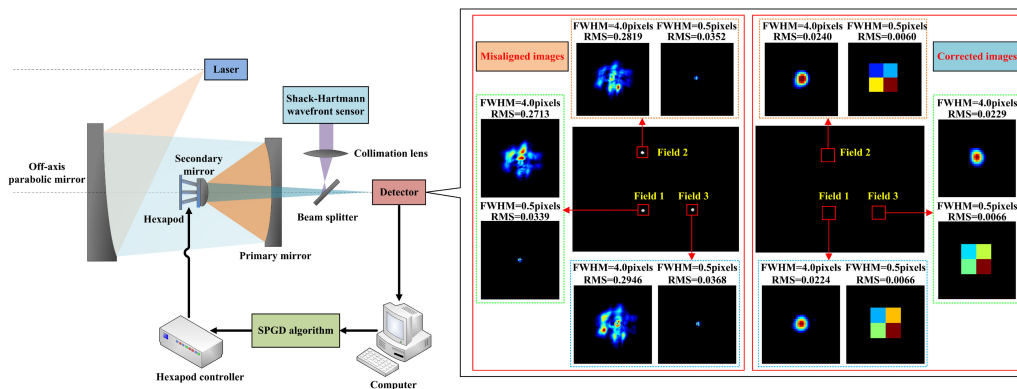
Min Li
Xin Liu
Ang Zhang
Hao Xian

Telescopes Alignment Using the Sharpness Function Method Based on Undersampled Images

Min Li [1,2,3] **Xin Liu,**[2] **Ang Zhang,**[1,2] **and Hao Xian**[1,2]

[1]Key Laboratory of Adaptive Optics, Chinese Academy of Sciences, Chengdu 610209, China
[2]Institute of Optics and Electronics, Chinese Academy of Sciences, Chengdu 610209, China
[3]University of Chinese Academy of Sciences, Beijing 100049, China

Abstract: In astronomy, the images are sometimes undersampled. In the previous research works, image reconstructions have to be employed to recover the lost information from a set of undersampled images to achieve a high-resolution image using dithering or drizzle methods, which increase the complexity of alignment processes and make the real-time correction impossible. In this paper, the telescope is aligned by changing the positions of the secondary mirror using sharpness function method combined with the stochastic parallel gradient descent algorithm based on both well-sampled and undersampled images without image reconstructions. To improve the accuracy and robustness of the alignment, a new metric called relative root mean square error is proposed. Both numerical simulations and experiments are implemented, and the alignment precisions are measured by wavefront residual errors using Shack–Hartmann wavefront sensors. The results show that the correction processes can converge stably and quickly whether the images are well-sampled or undersampled. In experiments, the average wavefront error is 0.0595 λ for undersampled images and 0.0548 λ for well-sampled images after the telescope alignment, indicating that the misalignments are well compensated for both well-sampled and undersampled images.

Index Terms: Telescope alignment, SPGD algorithm, relative RMS errors, under-sampled images.

1. Introduction

With the development of astronomy, the need for the high resolution, depth and breadth of astronomical observations grows rapidly [1]. To satisfy the demands, reflecting systems with large apertures and wide fields of view are commonly used, because they can get rid of the chromatic aberration completely. However, the precise alignment of these telescopes is not an easy job.

In the previous studies, there are many approaches to align telescopes [2]. All these methods can be divided into three categories and the most commonly used one is called the direct wavefront sensing (WFS) method [3]–[5], such as sensitive table method [6], merit function regression method [7], Shack-Hartmann wavefront sensing method [8], and computer-aided alignment (CAA) method [9]–[12], which needs to add additional optical components in the system to detect the wavefront errors, increasing the complexity of optical systems. What's more, there are no wavefront sensors in some applications, for example, the space telescopes, which limit the applications of this kind of

methods. The second kind of alignment methods named image-based wavefront sensing method can estimate the wavefront errors and misalignments of telescopes based on one or more focal or defocused images, such as phase retrieval (PR) method [13]–[15] and phase diversity (PD) method [16], [17]. The third kind of alignment methods is called sharpness function method, which can align telescopes by maximizing the sharpness functions of the far-field images using optimization algorithms. The second and third kinds of methods only need one or more detectors to achieve the focal and defocused images without adding other optical components, simplifying the measurement systems. However, in astronomy, the images are sometimes under-sampled due to the imperfect optics, finite detector arrays, and finite individual detector sizes. Nowhere is this problem more acute than on the Hubble Space Telescope (HST) [18], [19] and James Webb Space Telescope (JWST).

For the alignment of HST and JWST telescopes, the information lost from under-sampled images has to be reconstructed using dithering or drizzle method. Then the phase retrieval and phase diversity methods are used to estimate the wavefront errors from the reconstructed images [20]–[23]. The dithering method is one of the most popular image reconstruction methods based on several under-sampled images with low resolutions achieved by subpixel shifts of the detector to recover a high resolution image, which aims at solving the under-sampled problem of the HST telescope. It was used in a staring infrared imaging system to reduce the aliased signal energy by Joseph C. Gillette [24] in 1995 and further studied by Lauer in 1999 [25], who have been suggested for the linear combination of dithered images to reconstruct a high resolution image. Another image reconstruction method called drizzle method was proposed by Fruchter and Hook in 2002 [18] which was also known as Variable-Pixel Linear Reconstruction, focused on providing a flexible and general method of dithering image combination that produces high-resolution results without sacrificing the final signal-to-noise ratio. In recent years, a detector array with subpixel mismatch can substitute the shifts of CCD and the drizzling method has become a well-developed and widely used technology to reconstruct the under-sampled images. All the methods based on image reconstruction increase the complexity of alignment processes and make the real-time correction impossible.

In this paper, to simplify the measurement systems and realize the closed-loop alignment in real time, a sharpness function method combined with stochastic parallel gradient descent (SPGD) algorithm based on both well-sampled and under-sampled images is proposed. The sharpness function method is a wavefront sensor-less method [26]–[31] by maximizing the sharpness functions of images using optimization algorithms to correct the misalignments. Compared with the direct wavefront sensing method and image-based wavefront sensing method, this method only requires one detector placed in the focal plane to measure the sharpness of images in real time, and the misalignments are corrected by optimization algorithms without wavefront reconstructions. For the advantages of concise measurement systems and simple calculations, this method has broad applications. It can be used not only in the alignment of ground-based telescopes, but also to align the space telescopes.

There are many sharpness functions which are commonly used for the specific applications, such as the entire light intensity or partial intensity or strehl ratio and so on. In this paper, root mean square (RMS) radius is employed for the advantages of high stability and strong robustness. For telescopes with a narrow field of view and loose demanding image qualities, only on-axis field alignment can satisfy the requirements of the telescope performance, but for telescopes with a wide field of view and high demanding image qualities, images in the off-axis fields still carry large aberrations after the on-axis field alignment. To ensure the image qualities in the full field of view, a two-step alignment method is proposed. First, telescopes are aligned based on the sharpness functions of images obtained in on-axis field to correct the defocus and spherical aberrations. Then, telescopes are aligned based on the average sharpness functions of images achieved in both on-axis and off-axis fields to compensate coma and astigmatism aberrations. However, the results show that the changes of sharpness functions (RMS) are quite small for under-sampled images by 10^{-3} order of magnitudes, decreasing the sensitivity and accuracy of the alignment. What's more, the alignment process is affected easily by outside disturbance. To solve this problem, a new merit function called relative RMS error was presented and defined as the ratio of absolute RMS error

to the RMS values of designed images achieved in the designed working condition of telescopes. The absolute RMS errors are the differences of RMS between real images and designed images.

The paper is outlined as follows. In Section 2, the sharpness function method and Nyquist sampling theory are introduced briefly. In Section 3, both simulations and experiments are implemented. Sharpness function method combined with SPGD algorithm is used to align the telescopes based on both well-sampled and under-sampled images. At first, root mean square (RMS) radius of images is employed as the sharpness function. However, for under-sampled images, the changes of RMS are too small, decreasing the sensitivity and the precision of programs. To solve this problem, a new sharpness function called relative RMS error is proposed. To verify the accuracy, wavefront residual errors are measured by Shack-Hartmann wavefront sensors. In Section 4, the study conclusions and some suggestions for further research are given.

2. Theory

In this part, the alignment method based on the sharpness function combined with SPGD algorithm and the Nyquist sampling condition for telescopes are briefly introduced.

2.1 Telescope Alignment Method

Sharpness functions are used to estimate the image qualities to evaluate the performance of optical systems. There are many commonly used sharpness functions, such as the encircled energy, strehl ratio and so on. In this paper, the root mean square (RMS) radius is employed for the advantages of high stability and strong robustness and defined as follows [32].

$$J = \frac{\iint \sqrt{(x - x_0)^2 + (y - y_0)^2} I(x, y) dxdy}{\iint I(x, y) dxdy} \tag{1}$$

Where, (x, y) is the distribution coordinates of the detector. $I(x, y)$ is the light intensity on the pixel whose coordinate is (x, y) in the focal plane. (x_0, y_0) is the centroid of the light intensity distribution, defined as Eq. (2).

$$x_0 = \frac{\iint x I(x, y) dxdy}{\iint I(x, y) dxdy}, y_0 = \frac{\iint y I(x, y) dxdy}{\iint I(x, y) dxdy} \tag{2}$$

For the sharpness function method, the optimization algorithms are used to search for the best results. Many optimization algorithms were proposed in the past few years, for example, the Genetic Algorithm (GA) and Simulated Annealing (SA) algorithm. In this paper, SPGD algorithm [33], [34] is employed for the advantages of stable and quick convergence without falling into the local optimum as well as the strong robustness. The SPGD algorithm is a model-free iteration control method [35], which applies small random perturbations to all control parameters simultaneously and evaluates the gradient variation of the system performance metric (J) [36].

The iterative formula of SPGD algorithm is as follows [37], [38].

$$u^{k+1} = u^k - \gamma \bullet \delta J^k \bullet \delta u^k \tag{3}$$

Where, k is the number of iterations, and γ is the gain coefficient, the sign of which is determined by the sharpness functions. If the optimal object is the minimum of the sharpness functions, γ is positive. Otherwise, it will be negative.

u is the control variable. For two-mirror telescopes with large apertures and wide fields of view, the alignment is usually done [39] by applying tip/tilt and displacement corrections to the secondary mirror until the far-field image of a star acquires the shape of an airy disk, symmetrical in both shape and illumination. We are assuming here that the primary mirror is not adjustable, thus leaving all corrections to the secondary mirror [40]. The misalignments of the secondary mirror related to the primary mirror consist of six degrees of freedom, including decentration along x, y, z axis and tilt/tip about the three axes. Here, z axis is the optical axis of the system. The rotation about z axis has no

effect on the qualities of images, so it is usually ignored. All the five misalignments can introduce aberrations and degrade the image qualities. According to the vector wave aberration theory, the offsets along z axis (Dz) can introduce defocus and spherical aberrations, while offsets along x and y axis (Dx, Dy) as well as the tilt about *these two axes* (Tx, Ty) will introduce coma and astigmatism [41]. So, for telescope alignment, the control variables are composed of five degrees of freedom, including Dx, Dy, Dz, Tx, Ty, representing the decentration along x, y, z axis and the tilt about x and y axis.

$$u = [Dx, Dy, Dz, Tx, Ty] \tag{4}$$

In Eq. (3), δu is small random perturbations which has identical amplitudes and satisfies the Bernoulli probability distribution. δJ is the variation of the sharpness functions. To improve the accuracy of estimations, binary-side perturbation is used, which can be expressed as Eq. (5) [36].

$$\delta J = J(u + \delta u) - J(u - \delta u) = J_+ - J_- \tag{5}$$

The goal of SPGD method based on the far-field telescope image is to minimize the sharpness function J.

2.2 Nyquist Sampling Condition for Telescopes

According to the Rayleigh criterion, the resolution of telescopes is defined as Eq. (6).

$$\frac{\delta}{2} = \frac{1.22\lambda}{D} f_{telescope} = 1.22\lambda F^{\#} \tag{6}$$

Where, λ is the central wavelength of telescopes and δ is diameter of image spots. $F^{\#}$ is the F number of the optical system, defined as the ratio of the focal length $f_{telescope}$ to the optical apertures D.

The maximum spatial frequency of telescope systems is defined as Eq. (7),

$$v_{max} = \frac{2}{\delta} = \frac{1}{1.22\lambda F^{\#}} \tag{7}$$

For detectors, such as Change Coupled Device (CCD), supposing the interval of neighborhood pixels is $d \, \mu$m, the Nyquist frequency is shown as Eq. (8).

$$v_N = \frac{v_s}{2} = \frac{1}{2d} \quad \text{lp}/\mu\text{m} \tag{8}$$

Where, v_s is the sampling frequency of the detector, which is two times of the Nyquist frequency.

According to the Nyquist theorem, the Nyquist sampling frequency of detectors should be equal to or larger than the maximum spatial frequency of telescopes. Otherwise, the images will be under-sampled and aliasing will appear [42].

$$v_{max} \leq v_N \Rightarrow \delta \geq 4d \tag{9}$$

Equation (9) shows that the diameters of telescope spots should be equal to or larger than 4 pixels, otherwise the spots will be under-sampled.

3. Numerical Simulations and Experiments

3.1 Numerical Simulations

In numerical simulations, a Cassegrain telescope system with optical aperture as 1.76 m, full field of view as 0.7°, and central wavelength as 0.65 μm was used. Other parameters of the optical system are shown in Table 1.

Table 1 shows that the primary mirror (PM) was a parabolic reflector with conic of -1, semi-diameter of 880 mm and radius of -5400 mm. While the secondary mirror (SM) was a hyperbolic reflector with conic of -1.688, semi-diameter of 142.9 mm and radius of -938 mm. The distance

TABLE 1

Parameters of the Cassegrain Telescope System

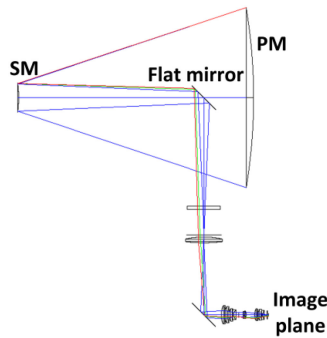| Surface	Semi-diameter / mm	Radius / mm	Thickness / mm	Conic
Primary mirror	880	-5400	-2292	-1
Secondary mirror	142.9	-938	1807	-1.688

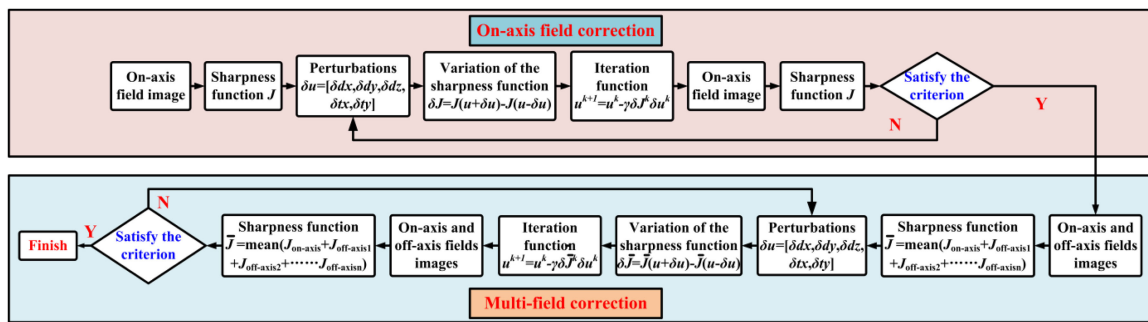Fig. 1. The Cassegrain telescope system.

Fig. 2. Alignment processes of the sharpness function method combined with SPGD algorithm.

between the primary and the secondary mirrors was -2292 mm. The telescope system is shown in Fig. 1.

For telescopes with a wide field of view, a two-step alignment method was proposed to ensure the image qualities in the full field of view. First, the misalignments were corrected based on the sharpness function of the on-axis field image to correct the defocus and spherical aberrations. Then, the misalignments were corrected based on the mean sharpness functions of both on-axis and off-axis fields images to correct the coma and astigmatism aberrations. In simulations, three fields of view were used including the on-axis field (0 field) with coordinate as (0°, 0°) and two off-axis fields (0.8 field, 1.0 field) with coordinate as (0°, −0.28°) and (−0.35°, 0°). The alignment processes are shown as Fig. 2.

To simulate the misalignments of telescopes, three sets of misaligned errors were given according to the practical applications, and each of them had five values corresponding to the five degrees of freedom of the secondary mirror. The misalignments are shown in Table 2.

In Table 2, the first and second sets of misalignments are large which may introduce various aberrations, while the third set of misalignments only gives a decentration along the optical axis, which may introduce defocus and spherical aberrations.

In this paper, the telescope was aligned based on both well-sampled and under-sampled images. As mentioned in Section 2.2, for well-sampled images, the diameters should be equal to or larger than 4 pixels. Otherwise, the images will be under-sampled. Here, the diameters of images were

TABLE 2
Misalignment Errors of the Secondary Mirror

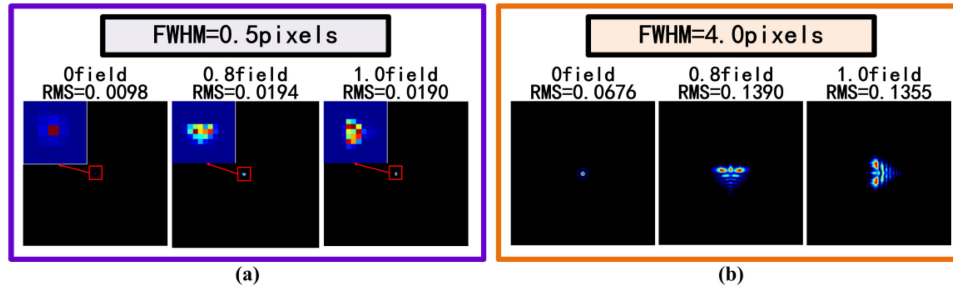| Number	Dx / μm	Dy / μm	Dz / μm	Tx / °	Ty / °
1	600	880	80	0.1	0.03
2	-500	-300	-60	-0.3	-0.1
3	0	0	40	0	0

Fig. 3. Designed images achieved in designed working conditions. (a) Designed images with FHWM as 0.5 pixels. (b) Designed images with FWHM as 4.0 pixels.

TABLE 3
Parameters of the Algorithm

Misalign-ments	Step size / δu					Image sizes	Gain coefficient / γ	
	δdx / mm	δdy / mm	δdz / mm	δtx / °	δty / °	n_0 / pixels	FWHM=0.5pixels	FWHM=4.0pixels
1	0.2	0.2	0.1	0.05	0.05			
2	0.2	0.2	0.1	0.04	0.04	200	5	1
3	0.1	0.1	0.05	0.01	0.01			

evaluated by the full width half maximum (FWHM). In simulations, the under-sampled images were obtained by pixel binning method with different under-sampled factors S. The bigger the under-sampled factors are, the more information will be lost. For detectors, the increase of under-sampled factors represents that the pixel sizes become larger. As examples, the FWHMs of well-sampled images used in this paper were 4 pixels. While the FWHMs of the under-sampled ones were 0.5 pixels.

The designed images obtained in the designed working condition without any misalignments are shown in Fig. 3.

As we can see from Fig. 3(b), the well-sampled designed image in the on-axis field of the telescope is almost a perfect airy spot, and images in off-axis fields only carry little aberrations. For under-sampled images in Fig. 3(a), the information is seriously lost. As a result, aberrations of the optical system cannot be exhibited obviously and accurately, which may decrease the accuracy of alignment processes.

In this paper, two sharpness functions were used to align the telescope, including the RMS and relative RMS errors.

First, the misalignments were corrected based on the sharpness function called RMS according to Fig. 2. The parameters of the algorithm are set as Table 3.

The alignment results are shown in Fig. 4.

Figure 4(a) and (b) show that the first and second sets of misaligned images bring large aberrations, including coma, astigmatism, spherical and defocus aberrations, causing the rapid deterioration of image qualities. While the third set of misalignments only introduces defocus and spherical
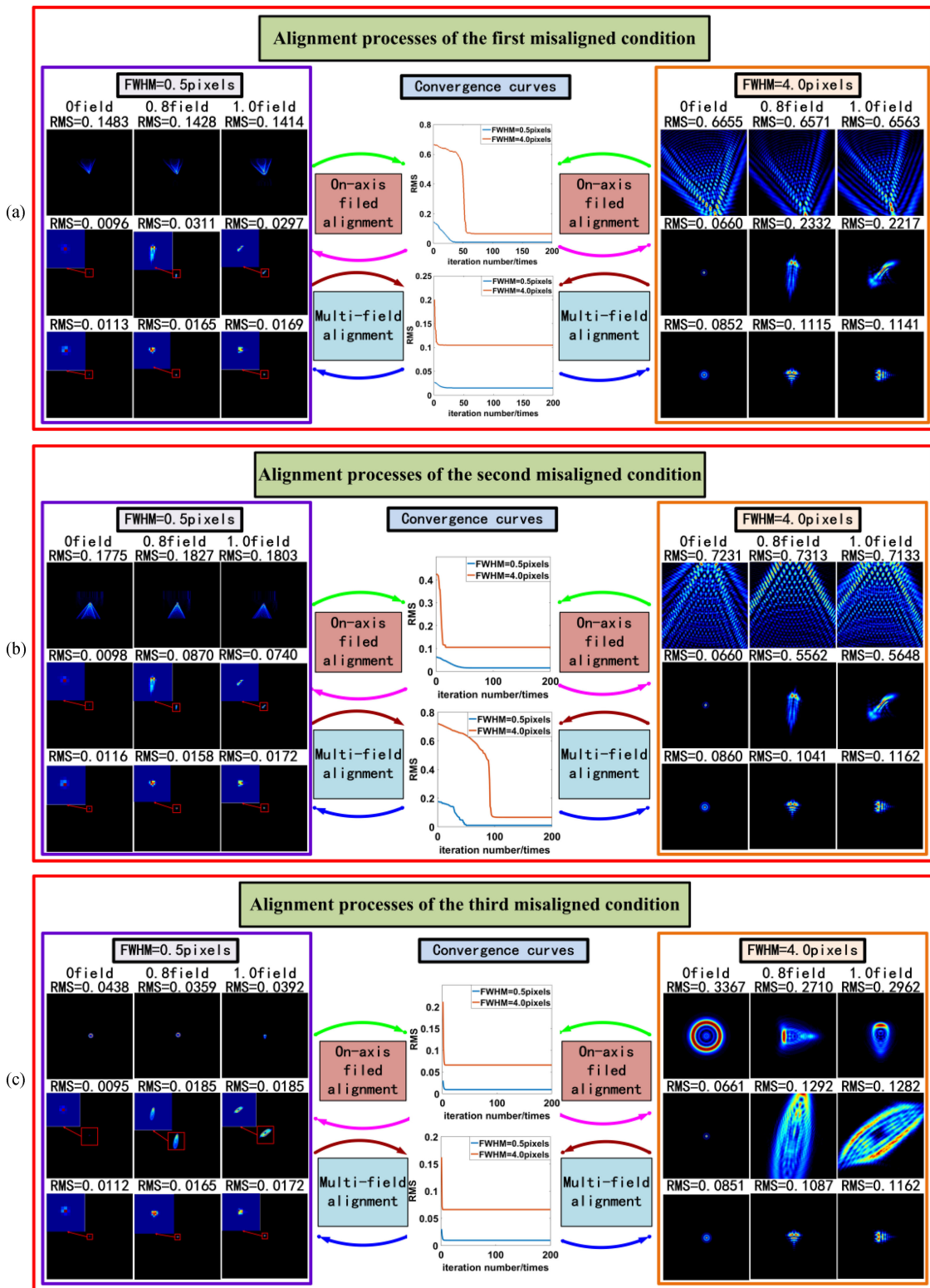
Fig. 4. Results of the telescope alignment based on both well-sampled and under-sampled images. (a) Results of the first misaligned condition. (b) Results of the second misaligned condition. (c) Results of the third misaligned condition.

aberrations with images dispersed. The results also indicate that after on-axis field alignment, the well-sampled and under-sampled images in the on-axis field are with the same shapes and intensity distributions as the designed images, demonstrating that the aberrations in on-axis field are well compensated. But for images in the off-axis fields, large aberrations still exist as the RMSs of spots are much larger than the designed ones if only aberrations in the on-axis field are corrected. However, after the multi-field alignment, images in both on-axis and off-axis fields carry little aberrations with almost the same shapes and intensity distributions as the designed ones, and the RMSs of images coincide with images achieved in the designed working condition of the telescope. As a result, to improve the telescope performance in the full field of view, aberrations in both on-axis and off-axis fields should be compensated.

As we can see from the convergence curves in Fig. 4, the alignment processes can converge quickly and stably whether the images are well-sampled or under-sampled, testifying the feasibility of our method. However, the final RMSs of under-sampled images are much smaller than the well-sampled images. One of the reasons responses for this phenomenon is that all the simulated images are with the same sizes $200 * 200$ pixels, the larger the under-sampled factor is, the less information the spots carries. So, the RMS becomes smaller with the decreases of FWHM. The reason why the image sizes are set as $200 * 200$ pixels is that according to the analysis, if the image sizes are less than $100 * 100$ pixels, the alignment processes will not converge with much information lost, while if the image sizes are larger than $400 * 400$ pixels, the alignment processes will not converge or converge slowly with poor precisions due to the small changes of RMS. To ensure the alignment processes converge quickly and stably, the image sizes are set as $200 * 200$ pixels.

Although the alignment processes can converge rapidly and stably and the misalignments are well corrected, the changes of RMS for under-sampled images are too small with 10^{-3} order of magnitudes, reducing the sensitivity and robustness of the alignment program. To solve this problem, a new sharpness function called relative RMS errors was proposed. It was defined as the ratio of the absolute RMS errors to the average RMS of designed images, and the absolute RMS errors were the differences between average RMS of real images and designed images.

$$relativeRMSerror = \frac{\overline{RMS}_{corrected} - \overline{RMS}_{designed}}{\overline{RMS}_{designed}} = \frac{absoluteRMSerror}{\overline{RMS}_{designed}} \qquad (10)$$

The misalignments were corrected according to Fig. 2 using the new sharpness function named relative RMS errors. The alignment results are shown in Fig. 5.

As we can see from the convergence curves in Fig. 5, the variation ranges of the new sharpness function become much broader than RMS, which only changes with 10^{-3} order of magnitudes for under-sampled images. The telescope alignment processes can converge quickly and stably for both well-sampled and under-sampled images according to the convergence curves. What's more, the final relative RMS errors for well-sampled and under-sampled images are consistent, indicating that the precisions of alignment based on under-sampled images are almost same with the well-sampled ones. Both the well-sampled and under-sampled images after multi-field alignment are with almost same shapes and intensity distributions as the designed images, demonstrating that the misalignments are well compensated. As the convergence curves shown in Fig. 5(c), the final relative RMS errors are smaller than zero after the multi-field alignment process, this is because our method using the optimization algorithm combined with the sharpness functions aims at finding the best positions of the seconday mirror to achieve a good image quality instead of the designed positions. Furthermore, the results of our method are not unique, because the misalignments corresponding to the five degrees of freedom of the secondary mirror are coupled with each other, for example, both the decentration along x axis and tilt about y axis can introduce coma and astigmatism aberrations, and the aberrations introduced by these two misalignments can be cancelled out by each other.

To compare the effects of these two sharpness functions, the three sets of misalignments were corrected using RMS and relative RMS errors as the sharpness functions respectively, and images
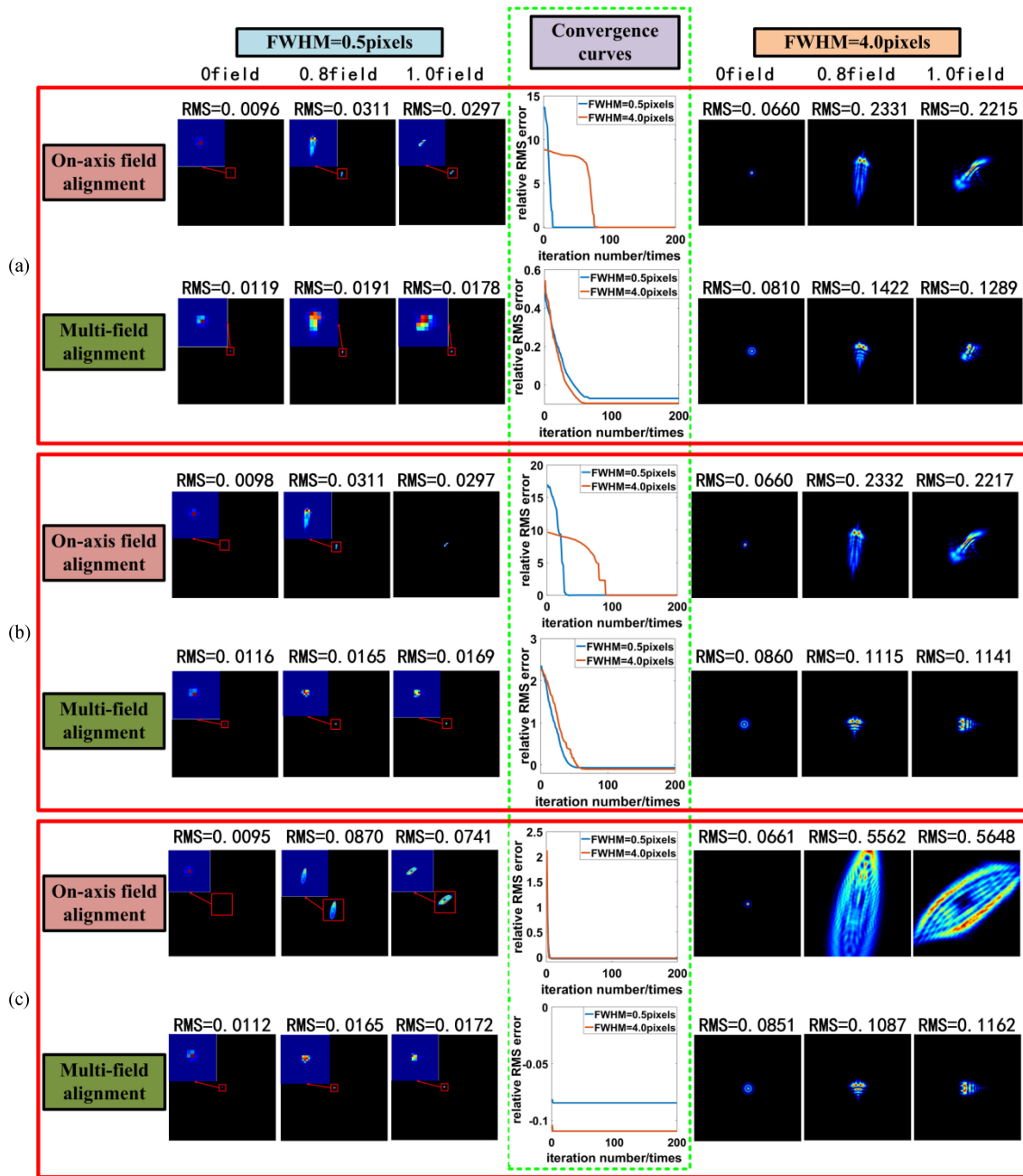
Fig. 5. Alignment processes based on the sharpness metric of relative RMS errors. (a) Results of the first misaligned condition. (b) Results of the second misaligned condition. (c) Results of the third misaligned condition.

with different FWHMs were used, including FWHM as 0.5, 1.0, 1.5, 2.0, 2.5, 3.0, 3.5, 4.0 pixels. The results of alignment were evaluated by ratio of the RMS differences between the corrected images and designed images to the RMS of the designed images, which are shown as Fig. 6.

As we can see from Fig. 6, the errors are smaller than zero which mean that the average RMSs of corrected images are smaller than the designed ones. This is because our method aims at finding the best positions of the secondary mirror to achieve a good image quality instead of the designed positions. So, the smaller the sharpness function is, the better performance the telescope
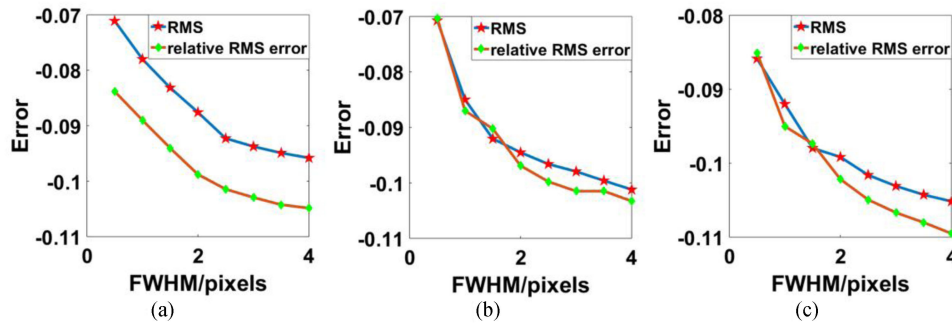
Fig. 6. Comparison of correction results with different under-sampled images. (a) Comparison of correction results for the first misaligned condition. (b) Comparison of correction results for the second misaligned condition. (c) Comparison of correction results for the third misaligned condition.
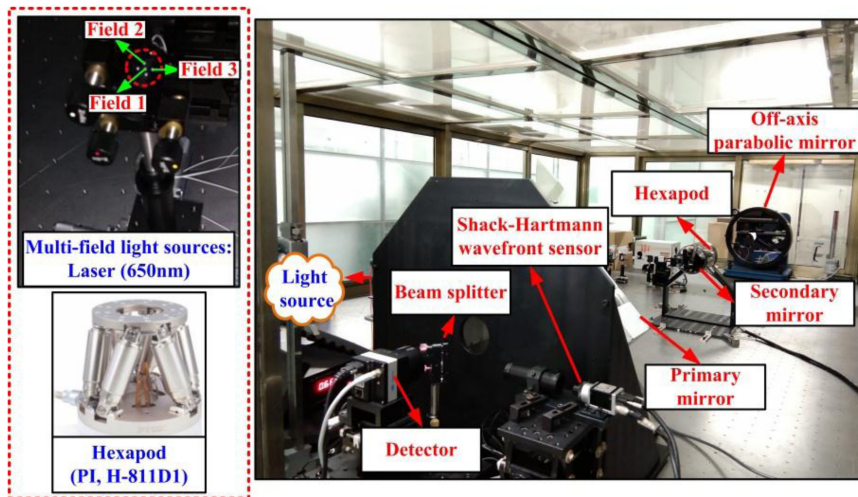

Fig. 7. The experiment system.

will have. Figure 6 also shows that with the increase of FWHMs, the absolute values of errors become larger, indicating that the RMS of corrected images is better than the designed ones and the alignment process is more accurate. In other words, the alignment process based on the well-sampled images is more precise compared with the under-sampled images. This is because the under-sampled images with much information lost cannot present the aberraitons competely and accurately, decreasing the alignment precisions. For the reason that the alignment results using the relative RMS errors as the sharpness function have higher accuracy than using RMS as the sharpness function, the telescope is aligned based on the relative RMS errors in experiments.

3.2 Experiments

According to the simulations, experiment system was set up. In experiments, a two-mirror Cassegrain telescope with a parabolic primary mirror whose radius was -3300 mm and optical aperture was 400 mm and a hyperbolic secondary mirror whose radius was -1186 mm and the aspheric coefficient was -3.094 was used. The experiment system is shown as Fig. 7.

The full field of view of the experiment system was $0.3°$. In the experiments, three fields of view were used, including the on-axis field (field 1) with coordinate as $(0°, 0°)$ and two off-axis fields (field 2, field 3) with coordinates as $(0°, 0.1°)$ and $(0.1°, 0°)$. Point sources with wavelength of 650 nm were employed. The laser beams were collimated by the off-axis parabolic (OAP) mirror (OAP-100-02-16SQ) and became parallel light, which were separated by the splitter mirror after

TABLE 4
Parameters of the Experiment Program

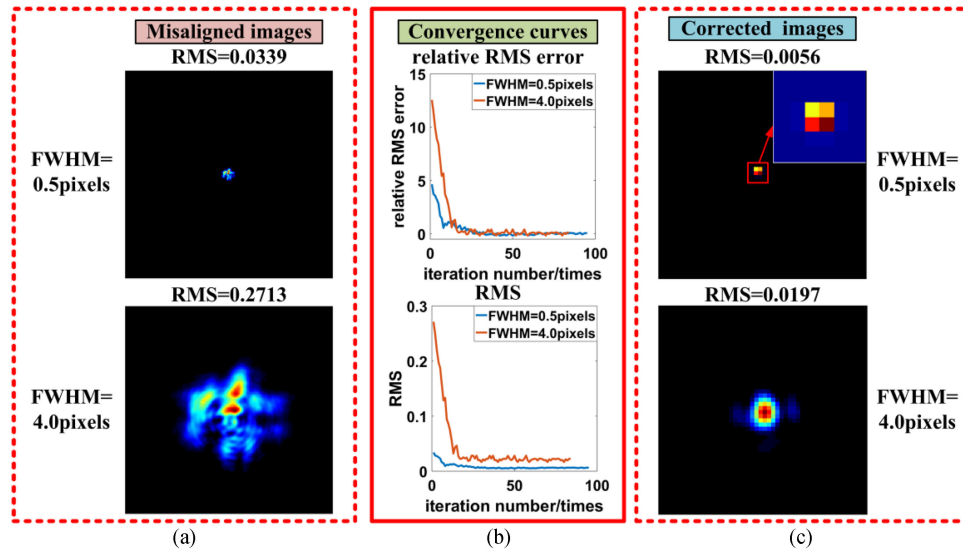|	Step size / δu				Image sizes	Iteration number	Gain coefficient / γ	
δdx / mm	δdy / mm	δdz / mm	δtx / °	δty / °	n_0 / pixels	n / times	FWHM=0.5pixels	FWHM=4.0pixels
0.1	0.08	0.04	0.004	-0.005	100	100	10	10

Fig. 8. Images in on-axis field achieved before and after the on-axis alignment. (a) Misaligned images with FWHM as 0.5 pixels and 4.0 pixels. (b) Convergence curves. (c) Corrected images with FWHM as 0.5 pixels and 4.0 pixels.

reflected from the primary mirror (PM) and the secondary mirror (SM). One beam arrived to the far-field detector (Baumer, LXG-200M), whose pixel size was 6.4 μm and resolution was $5120 * 3840$ pixels to record images, and the other beam reached to the Shack-Hartmann detector (Basler, acA1600-20gm), whose pixel size was 4.4 μm and resolution was $1236 * 1626$ pixels to measure the wavefront residual errors after misalignments correction. The focal length of micro lens in the wavefront sensor was 5 mm.

After the experiment system was set up, the misalignments between the primary and secondary mirrors were corrected based on the well-sampled and under-sampled images achieved in the far-field detector. In this paper, the well-sampled images with FWHM of 4 pixels and under-sampled images with FWHM of 0.5 pixels were used as examples. The positions of the secondary mirror were changed by the Hexapod (PI, H-811D1), which was a six-degree-of-freedom motion platform, including the linear motion along the x, y, z axis, as well as the rotation along the three axes. The Hexapod can travel along the x, y, z axis with a minimum displacement of 0.25 μm and rotate about three axes with a minimum rotation of 3 μrad. The telescope was aligned according to the Fig. 2. The parameters of the algorithm are set as Table 4.

The on-axis field images achieved before and after the on-axis field alignment are shown in Fig. 8.

Figure 8(a) shows that the misaligned images are dispersed with large aberrations. However, the under-sampled aberrated images with much information lost cannot express the aberrations completely and accurately, which may decrease the alignment precision. According to the simulations, using relative RMS error as the sharpness function can improve the accuracy of the alignment. So in experiments, the telescope is aligned based on the relative RMS errors, the changes of RMS are also calculated and shown in Fig. 8(b). The convergence curves show that the alignment process can converge stably and rapidly with qualities of on-axis field images improved greatly. To ensure
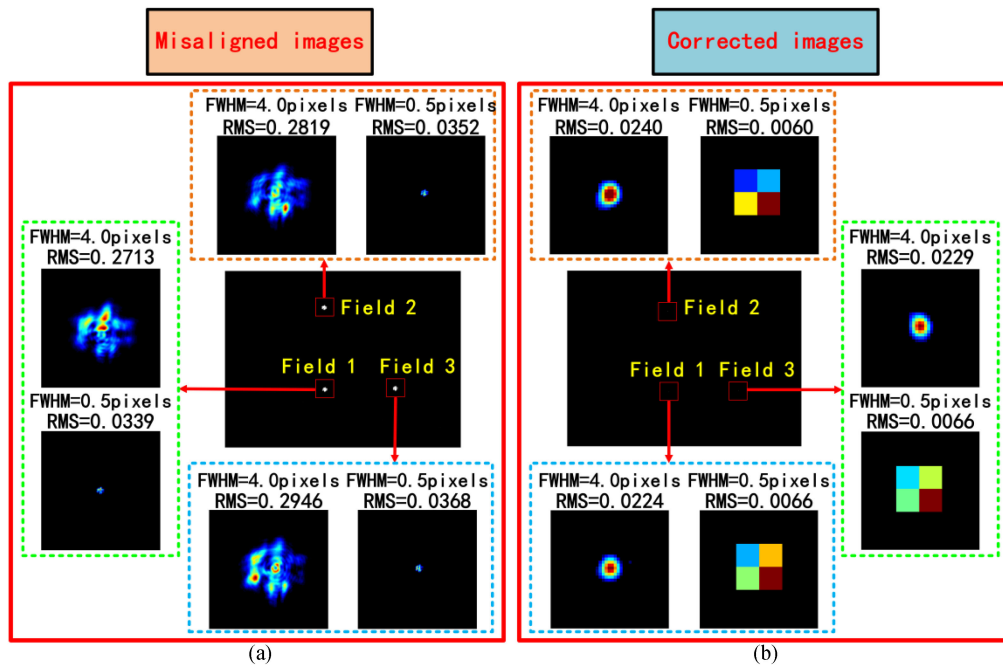
Fig. 9. Multi-field images achieved before and after alignment. (a) Misaligned images. (b) Corrected images.

TABLE 5
RMS and Wavefront Residual Errors

RMS and WRE		FWHM=0.5pixels			FWHM=4.0pixels		
		Field 1	Field 2	Field 3	Field 1	Field 2	Field 3
RMS	Designed images	0.0062	0.0063	0.0068	0.0220	0.0254	0.0239
	Misaligned images	0.0339	0.0352	0.0368	0.2713	0.2819	0.2946
	Corrected images	0.0066	0.0060	0.0066	0.0224	0.0240	0.0229
WRE / λ	Designed conditions	0	0.0302	0.0302	0	0.0302	0.0302
	Corrected conditions	0.0624	0.0598	0.0563	0.0516	0.0589	0.0538

the image qualities in the full field of view, multi-field alignment has to be carried out. The results are shown as Fig. 9.

Figure 9(a) shows that the images in the misaligned working condition of the telescope carry large aberrations including defocus, coma, astigmatism and spherical aberrations with big RMS of spots in both on-axis and off-axis fields. The shapes and intensity distributions of under-sampled misaligned images with FWHM of 0.5 pixels cannot express the aberrations of the optical system clearly and accurately for the reason that some information is seriously lost, and this may decrease the precision of the alignment. Figure 9(b) demonstrates that qualities of images after correction have improved greatly as the RMS decreases and the energy distributions become concentrated whether the images are well-sampled with FWHM as 4 pixels or under-sampled with FWHM as 0.5 pixels. To verify the precision of the alignment, wavefront residual errors (WRE) are measured using Shack-Hartmann wavefront sensors. The RMS and WRE after telescope alignment are calculated and shown in Table 5.

Table 5 shows that for both well-sampled and under-sampled images, the RMS values after telescope alignment are consistent with the designed ones, indicating that the misalignments are well compensated. According to the wavefront residual errors of the optical system, the precision of

the alignment based on the under-sampled images is slightly worse than the well-sampled images. That is because for under-sampled images, some information is lost and the images cannot exhibit the aberrations completely. Even though, the average wavefront error of three fields of view is about 0.0595 λ for under-sampled images and 0.0548 λ for well-sampled images, both of which are less than $\lambda/10$, satisfying the requirements of image qualities.

4. Conclusion

The accuracy of alignment is a key factor to determine the performance of telescopes. However, the under-sampled images with some information lost may decrease the precision of the alignment. In the previous studies, image reconstruction has to be used to recover the information lost from the under-sampled images, which increases the complexity of alignment processes and makes the real-time alignment impossible. In this paper, the sharpness function method combined with SPGD algorithm is used to align the telescopes based on both well-sampled and under-sampled images without doing the image reconstructions, which can simplify the alignment processes and realize closed-loop corrections in real time. For large aperture telescopes, the primary mirror is usually large and complex, so the misalignments are compensated by changing the positions of the secondary mirror. Both simulations and experiments are implemented. In simulations, two sharpness functions including the RMS and relative RMS errors were used. The results show that the alignment program can converge quickly and stably for the two sharpness functions. Shapes and intensity distributions of corrected images are almost same with the designed ones, indicating that the telescope is well aligned. But compared with RMS, the relative RMS errors have higher accuracy and better stability. To verify the effects of the alignment, wavefront residual errors are measured using Shack-Hartmann wavefront sensors in experiments. The results show that the wavefront residual errors for under-sampled images are slightly worse than the well-sampled images. However, the average wavefront error is about 0.0595 λ for under-sampled images and 0.0548 λ for well-sampled images, both of which are less than $\lambda/10$, satisfying the requirements of image qualities. The simulations and experiments certified that our method is feasible and reliable for telescope alignment whether the images are well-sampled or under-sampled.

References

[1] Z. Y. Gu, C. X. Yan, and Y. Wang, "Alignment of a three-mirror anastigmatic telescope using nodal aberration theory," *Opt. Exp.*, vol. 23, no. 19, pp. 25182–25201, 2015.

[2] E. Luna, S. Zazueta, and L. Gutierrez, "An innovative method for the alignment of astronomical telescopes," *Publications Astronomical Soc. Pac.*, vol. 113, pp. 379–384, 2001.

[3] J. M. Beckers, "Adaptive optics for astronomy: principles, performance, and applications," *Annu. Rev. Astronomy Astrophys.*, vol. 31, pp. 13–62, 1993.

[4] J. J. Kim, D. C. Burtz, and B. N. Agrawal, "Wavefront correction of optical beam for large space mirrors using robust control techniques," *Acta Astronautica*, vol. 68, pp. 141–148, 2011.

[5] H. Lee, G. B. Dalton, I. A. J. Tosh, and S. W. Kim, "Computer-guided alignment II: Optical system alignment using differential wavefront sampling," *Opt. Exp.*, vol. 15, no. 23, pp. 15424–15437, 2007.

[6] J. W. Figoski, T. E. Shrode, and G. F. Moore, "Computer-aided alignment of a wide-field, three-mirror, unobscured, high-resolution sensor," *Proc. SPIE*, vol. 1049, pp. 166–178, 1989.

[7] S. Kim, H. S. Yang, Y. W. Lee, and S. W. Kim, "Merit function regression method for efficient alignment control of two-mirror optical systems," *Opt. Exp.*, vol. 15, no. 8, pp. 5059–5068, 2007.

[8] D. C. Zimmerman, "Feasibility studies for the alignment of the thirty meter telescope," *Appl. Opt.*, vol. 49, no. 18, pp. 3485–3498, 2010.

[9] Y. H. Lee, "Alignment of an off-axis parabolic mirror with two parallel He-Ne laser beams," *Opt. Eng.*, vol. 31, no. 11, pp. 2287–2292, 1992.

[10] M. R. Descour, M. R. Willer, D. S. Clarke, and C. E. Volin, "Misalignment modes in high performance optical systems," *Opt. Eng.*, vol. 39, no. 7, pp. 1737–1747, 2000.

[11] Z. S. Gao, L. Chen, S. Z. Zhou, and R. H. Zhu, "Computer aided alignment for a reference transmission sphere of an interferometer," *Opt. Eng.*, vol. 43, no. 1, pp. 69–74, 2004.

[12] B. Wang, S. L. Jiang, and T. Qiu, "Study on computer-aided alignment method of cassegrain system," *Proc. SPIE*, vol. 7654, pp. 674–679,2010.

[13] R. A. Gonsalves, "Phase retrieval from modulus data," *J. Opt. Soc. Amer.*, vol. 66, no. 9, pp. 961–964, 1976.

[14] J. Fienup, "Phase-retrieval algorithms for complicated optical system," *Appl. Opt.*, vol. 32, no. 10, pp. 1737–1746, 1993.

[15] R. Gerchberg and W. Saxton, "Phase determination for image and diffraction plane pictures in the electron microscope," *Optik*, vol. 35, no. 3, pp. 275–284, 1971.
[16] R. G. Paxman, T. J. Schulz, and J. R. Fienup, "Joint estimation of object and aberrations by using phase diversity," *J. Opt. Soc. Amer. A*, vol. 9, no. 7, pp. 1072–1085, 1992.
[17] M. Bolcar and J. Fienup, "Sub-aperture piston phase diversity for segmented and multi-aperture systems," *Appl. Opt.*, vol. 48, no. 1, pp. A5–A12, 2009.
[18] A. S. Fruchter and R. N. Hook, "Drizzle: A method for the linear reconstruction of undersampled images," *Astronomical Soc. Pac.*, vol. 114, pp. 144–152, 2002.
[19] L. D. Grey, "Control and alignment of the hubble space telescope," *Proc. SPIE*, vol. 0628, pp. 443–450,1986.
[20] J. S. Smith, D. L. Aronstein, and B. H. Dean, "Phase retrieval on broadband and under-sampled images for the JWST testbed telescope," *Proc. SPIE*, vol. 7436, pp. 7436–7448, 2009.
[21] D. S. Acton, J. S. Knight, A. Contos, S. Grimaldi, and J. Terry, "Wavefront sensing and controls for the james webb space telescope," *Proc. SPIE*, vol. 8442, 2012, Art. no. 84422H.
[22] T. Greene *et al.*, "NIRCam: development and testing of the JWST near-infrared camera," *Proc. SPIE*, vol. 7731, 2010, Art. no. 77310C.
[23] D. S. Acton and J. S. Knight, "Multi-field alignment of the james webb space telescope," *Proc. SPIE*, vol. 8442, pp. 121–131,2012.
[24] J. C. Gillette, T. M. Stadtmiller, and R. C. Hardie, "Aliasing reduction in staring infrared imagers utilizing subpixel techniques," *Opt. Eng.*, vol. 34, no. 11, pp. 3130–3137, 1995.
[25] T. R. Lauer, "The photometry of undersampled point-spread functions," *Publications Astronomical Soc. Pac.*, vol. 111, pp. 1434–1443, 1999.
[26] R. A. Muller and A. Buffington, "Real-time correction of atmospherically degraded telescope images through image sharpening," *J. Opt. Soc. Amer.*, vol. 64, no. 9, pp. 1200–1210, 1974.
[27] M. A. Vorontsov, G. W. Carhart, D. V. Pruidze, J. C. Ricklin, and D. G. Voelz, "Image quality criteria for an adaptive imaging system based on statistical analysis of the speckle field," *J. Opt. Soc. Amer. A*, vol. 13, no. 7, pp. 1456–1466, 1996.
[28] J. R. Fienup and J. J Miller, "Aberration corrected by maximizing generalized sharpness metrics," *J. Opt. Soc. Amer. A*, vol. 20, no. 4, pp. 609–620, 2003.
[29] B. Dong and J. Yu, "Hybrid approach used for extended image-based wavefront sensor-less adaptive optics," *Opt. Lett.*, vol. 13, no. 4, 2015, Art. no. 041101.
[30] H. Z. Yang, X. Y. Li, and W. H. Jiang, "Simulation and analysis of stochastic parallel gradient descent control algorithm for adaptive optics system," *Acta Opt. Sin.*, vol. 27, no. 8, pp. 1355–1363, 2007.
[31] L. F. Zhou *et al.*, "Experimental research of alignment error correction by aspheric mirror based on the function of imaging quality," *Acta Phys. Sin.*, vol. 65, no. 13, pp. 1–10, 2016.
[32] H. Yang, X. Li, C. Gong, and W. Jiang, "Restoration of turbulence-degraded extended object using the stochastic parallel gradient descent algorithm: Numerical simulation," *Opt. Exp.*, vol. 17, no. 5, pp. 3052–3062, 2009.
[33] M. A. Vorontsov and G. W. Carhart, "Adaptive optics based on analog parallel stochastic optimization: Analysis and experimental demonstration," *J. Opt. Soc. Amer. A*, vol. 17, no. 8, pp. 1440–1453, 2000.
[34] M. A. Vorontsov and G. W. Carhart, "Adaptive phase-distortion correction based on parallel gradient-descent optimization," *Opt. Lett.*, vol. 22, no. 12, pp. 907–909, 1997.
[35] Q. Fu, J. U. Pott, F. Shen, C. H. Rao, and X. Y. Li, "Stochastic parallel gradient descent optimization based on decoupling of the software and hardware," *Opt. Commun.*, vol. 310, pp. 138–149, 2014.
[36] B. Dong, D. Q. Ren, and X. Zhang, "Stochastic parallel gradient descent based adaptive optics used for a high contrast imaging coronagraph," *Res. Astronomy Astrophys.*, vol. 11, no. 8, pp. 997–1002, 2011.
[37] X. L. Wang, P. Zhou, Y. X. Ma, J. Y. Leng, X. J. Xu, and Z. J. Liu, "Active phasing a nine-element 1.14 kW all-fiber two-tone MOPA array using SPGD algorithm," *Opt. Lett.*, vol. 36, no. 16, pp. 3121–3123, 2011.
[38] C. Geng, W. Luo, Y. Tan, H. M. Liu, J. B. Mu, and X. Y. Li, "Experimental demonstration of using divergence cost-function in SPGD algorithm for coherent beam combining with tip/tilt control," *Opt. Exp.*, vol. 21, no. 21, pp. 25045–25055, 2013.
[39] R. N. Wilson, *Reflecting Telescope Optics*, 7th ed. London, U.K.: Cambridge Univ. Press, 2005.
[40] E. Luna, A. Cordero, J. Valdez, L. Gutie´rrez, and L. Salas, "Telescope alignment by out-of-focus stellar image analysis," *Publications Astronomical Soc. Pac.*, vol. 111, pp. 104–110, 1999.
[41] D. J. Schroeder, *Astronomical Optics*. San Diego, CA, USA: Academic, 2000, pp. 48–69.
[42] M. J. Fox, D. G. Voelz, and R. R. Shannon, "Image reconstruction from an undersampled focal plane using a sparse telescope array," *Opt. Eng.*, vol. 33, no. 10, pp. 3272–3282, 1994.